Semitransparent thermophotovoltaics for efficient utilization of moderate temperature thermal radiation

Tobias Burger^{1,+}, Bosun Roy-Layinde^{1,+}, Rebecca Lentz², Zachary Berquist¹,

Stephen R. Forrest^{2,3,4}, and Andrej Lenert^{*,1}

¹Department of Chemical Engineering

²Department of Electrical Engineering and Computer Science

³Department of Materials Science and Engineering

⁴Department of Physics

⁺These authors contributed equally: Tobias Burger, Bosun Roy-Layinde

University of Michigan, Ann Arbor, MI, 48109, USA

*Corresponding author: <u>alenert@umich.edu</u>

Classification: Engineering

Keywords: thermophotovoltaics, waste heat recovery, concentrating solar thermal, nuclear generator

Abstract

Recent advances in thermophotovoltaic (TPV) power generation have produced notable gains in efficiency, particularly at very high emitter temperatures. However, there remains substantial room for improving TPV conversion of waste, solar, and nuclear heat streams at temperatures below 1100°C. Here, we demonstrate the concept of transmissive spectral control that enables efficient recuperation of below-bandgap photons by allowing them to transmit through the cell to be absorbed by a secondary emitter. We fabricate a semitransparent TPV cell consisting of a thin InGaAs/InP heterojunction membrane supported by an infrared-transparent heat-conducting substrate. The device absorbs less than 1% of below bandgap radiation, resulting in a TPV efficiency of 32.5% at an emitter temperature of 1036°C. To our knowledge, this represents an 8% absolute improvement (~33% relative) in efficiency relative to the best TPV devices at such low temperatures. By enabling near-zero photon loss, the semitransparent architecture facilitates high TPV efficiencies over a wide range of applications.

Significance statement

Thermophotovoltaic (TPV) conversion offers a promising solid-state alternative to mechanical heat engines. Still, at temperatures compatible with the utilization of waste, solar, and nuclear heat, TPV efficiencies remain relatively low. This inefficiency is due to a red-shifted emission spectrum, which increases the fraction of heat transferred to the photovoltaic cell by low-energy photons. Here we demonstrate an infrared-transparent cell that uses a secondary thermal emitter, situated at the rear of the cell, to capture >99% of these photons. The architecture leverages a unique property of TPVs: the cell can be surrounded by radiation sources, unlike a solar cell. Experiments show TPV efficiencies of 32% at ~1000°C and additional modeling suggests 45% is possible even at ~800°C.

Introduction

The performance of thermophotovoltaic (TPV) cells has increased substantially over the last several years, with reports of TPV efficiency surpassing 30% using single-junction cells (1–5), and 40% using tandems (6). These gains have been demonstrated using group III-V semiconductors (*e.g.*, In_{0.53}Ga_{0.47}As lattice matched to InP) with wider bandgaps compared to conventional Sb-based TPV cells. Although these materials exhibit advantageous optical and charge carrier collection properties, they typically require emitter temperatures (*Th*) above 1200°C (5). Applications in stationary energy storage using thermal batteries may support extreme emitter temperatures as high as 2400°C, however, a wide range of thermal sources are at temperatures below 1100°C, including waste (7–9), concentrating solar (10–17), and nuclear (18) heat. In particular, the cement, chemical, iron and steel industries represent a large fraction of global industrial energy use and emissions with substantial waste heat streams at temperatures ranging from 700 to 1100°C.

Translating recent improvements in cell performance to waste heat, solar thermal, and nuclear applications is challenging since lower temperatures introduce substantial spectral (photon) and charge carrier losses (19). This can be appreciated by noting that TPV efficiency (η_{TPV}) is a product of spectral management ($SE \cdot IQE$) and charge management ($VF \cdot FF$) efficiencies (19). Here, SE, IQE, VF and FF are the spectral and internal quantum efficiencies, and the voltage and fill factors, respectively. Lower temperature emitters radiate a larger fraction of power at energies below the cell bandgap, resulting in lower SE. The conventional solution to this problem is to decrease the cell bandgap using Sb-based III-Vs; however, the voltage penalties associated with non-radiative recombination are prohibitively large in these materials, which results in poor charge

management. Alternatively, light management techniques that suppress below-bandgap (i.e., out-of-band) absorptance (*Aout*) can enable the use of highly efficient III-V absorbers, such as In_{0.53}Ga_{0.47}As (bandgap of 0.74 eV), by maintaining high spectral efficiency at lower emitter temperatures.

Existing techniques for suppressing below-bandgap radiative transfer in TPVs can be broadly categorized as emissive and reflective. Figure 1 shows the spectral efficiency corresponding to the best measured In_{0.53}Ga_{0.47}As (InGaAs) TPV efficiencies at moderate-to-low emission temperatures. The lowest SE region corresponds to selective emitters (19) that are designed to preferentially emit above-bandgap radiation while suppressing below-bandgap emission (20, 21). Although these emitters have demonstrated A_{out} as low as 7% at room temperature (22), the emissive properties are generally much higher (>14%) when characterized at the appropriate operating temperature (19, 23–25). In contrast, cells with conventional rear mirrors exhibit A_{out} as low as 5% (1, 3, 6, 26–29). These cells reflect below-bandgap radiation back to the emitter, which re-heats the emitter and facilitates recuperation of otherwise unusable power. Beyond conventional rear mirrors, cells that feature a low-index layer between the absorber and the rear metal, including patterned dielectric back contact (4) and air-bridge cells (2, 30), have enabled Aout as low as 2% (integrated from 0° to 90° incidence angle). Despite these recent advances in spectral management, a device that suppresses below-bandgap transfer with $A_{out} < 1.5\%$ has yet to be demonstrated. Accessing this regime would enable TPV cells based on InGaAs to maintain high efficiencies at temperatures relevant to conversion of waste, solar, and nuclear heat.

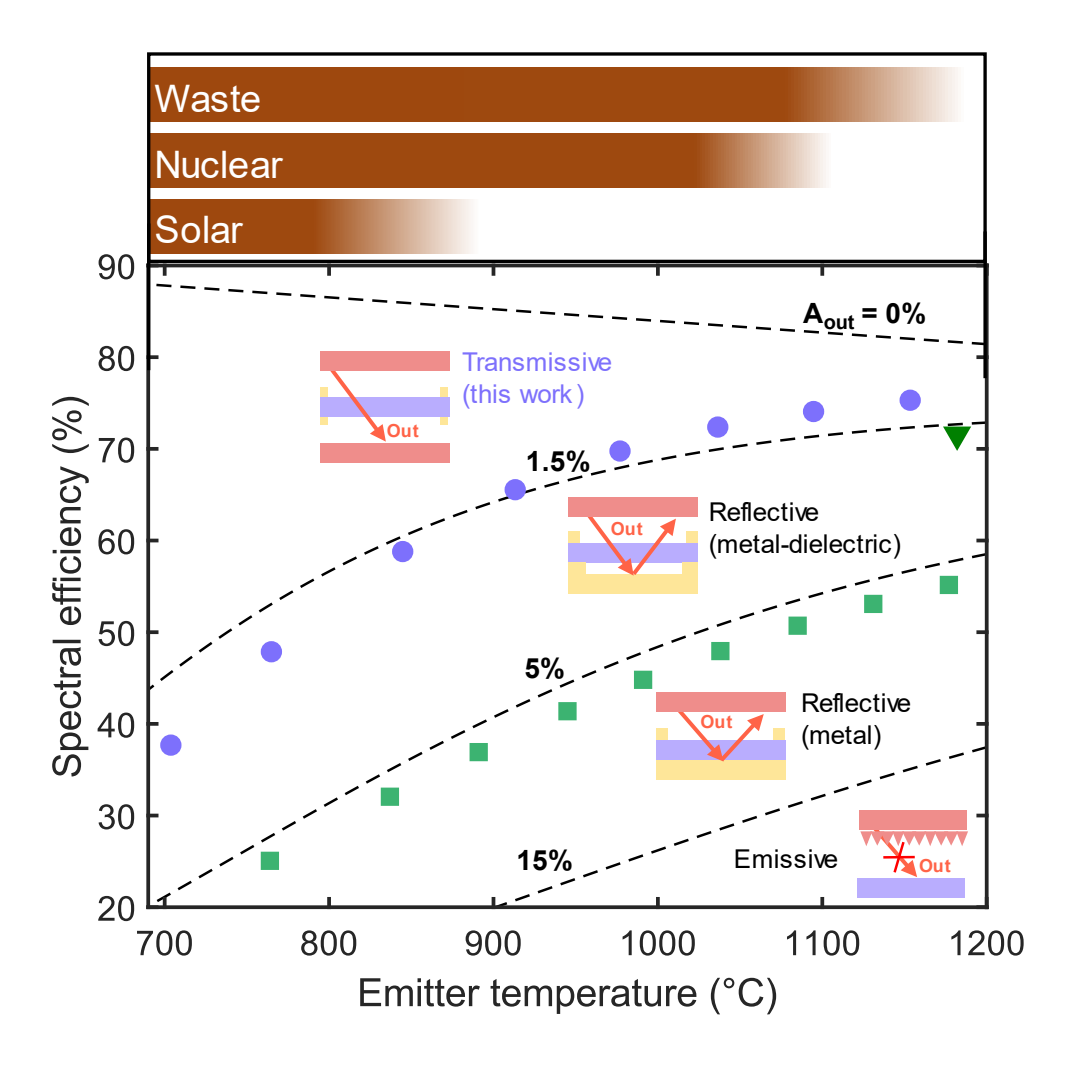


Figure 1. Current performance in spectral control at moderate-to-low emitter temperatures. Spectral efficiency (SE) at emitter temperatures relevant to applications in conversion of waste, solar, and nuclear heat. Out-of-band (i.e., below-bandgap) absorptance $A_{out} > 15\%$, $5 > A_{out} > 15\%$ and $1 > A_{out} > 2\%$, are characteristic of spectral performance achieved through use of selective emitters, reflective metal (square (28)) and metal-dielectric (triangle (2)) rear mirrors, respectively. $A_{out} < 1.5\%$ indicates the target range for the semitransparent cells described in this work. Spectral control strategies are depicted as inset schematics. SE curves are generated for $E_g = 0.74$ eV and in-band absorptance of 0.7. The top curve indicates SE in the radiative limit ($A_{out} = 0$).

Here we demonstrate the concept of transmissive spectral control that enables wavelength-selective radiative transfer with $A_{out} < 1.5\%$ and high TPV efficiency at moderate-to-low emission temperatures. The concept features a symmetric infrared-transparent photovoltaic cell that is situated between two thermal emitters and is thermally grounded by heat sinks on either edge, as shown in Figure 2. Surrounding the cell by the emission source is possible in TPVs, unlike in solar

cells, because the heat source is local (though, this unique feature has not been explored in prior TPV work). In this configuration, emitted below-bandgap photons transmit through the cell and are absorbed by the thermal emitter on the opposite side, and vice versa. Due to this symmetry, the net movement of photons is zero along the centerline of the cells. This implies that the centerlines act as perfect broadband reflectors, unlike dielectric and metal mirrors which are limited by bandwidth or intrinsic absorption (associated with finite electrical conductivity), respectively.

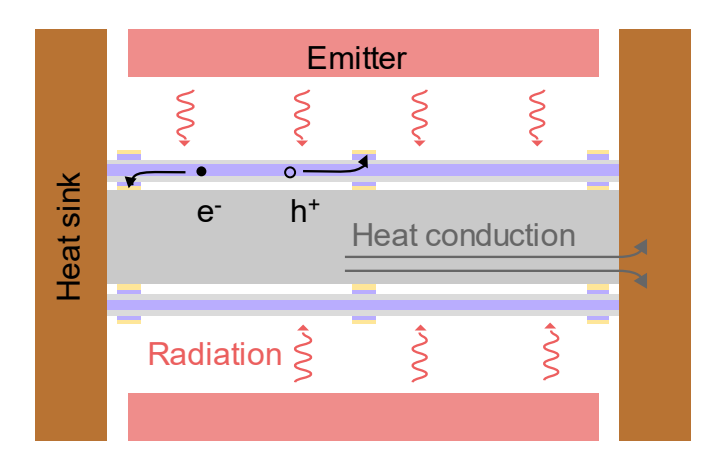


Figure 2. The semitransparent cell concept. Heat flows and carrier transport depicted in a two-dimensional projection of a symmetric TPV system that uses a hot emitter at the rear to capture transmitted below-bandgap photons. Above-bandgap photons excite electron-hole pairs in the absorber, which are separated and extracted at the contacts. Below-bandgap radiation transmits through the cell and is absorbed by the thermal emitter on the opposite side. Waste heat is conducted laterally along the length of the transparent substrate to the conductive heat sinks.

We demonstrate the concept by fabricating a semitransparent TPV cell consisting of a thin InGaAs/InP heterojunction membrane supported by an infrared-transparent heat-conducting substrate. The device builds upon our recent demonstration of air-bridge TPV cells that achieved power conversion efficiencies of 32% at an emitter temperature of ~1200°C (2). The air-bridge cell, however, exhibited $A_{out} \approx 2\%$ when integrated over all incidence angles, mainly due to relatively high absorption in the Au mirror at oblique angles. To overcome this limitation, the

semitransparent device eliminates the Au mirror and retains a transparent substrate ("fin") that allows transmission of thermal radiation. Owing to minimal photon loss (\sim 1%), the InGaAs cell demonstrated here achieves 72.2 \pm 0.2% spectral efficiency and 32.5 \pm 0.1% TPV efficiency at an emitter temperature of 1036°C. The latter result represents an 8% absolute improvement (\sim 33% relative) over previously measured cells at comparable temperatures (28). We expect that the device architecture introduced here could be broadly deployed to minimize optical losses and enable the use of wider bandgap cells, with key applications in clean energy and industrial waste heat recovery.

Results

To reach high TPV efficiency at lower emitter temperatures, the semitransparent device must combine efficient electrical and thermal management with near-zero photon losses. To this end, the design of the cell, gridlines, and substrate should minimize absorption of below-bandgap photons without degrading other performance characteristics.

We demonstrate a semitransparent TPV cell consisting of a thin InGaAs/InP heterojunction with a Au electrode grid matched to a similar grid on the Si substrate, as shown in Figure 3a. The Au patterns are aligned and cold-weld bonded using a flip chip and wafer bonding tool (see Methods). The process retains a 570 nm air-gap while allowing light to transmit through the substrate between the grid lines. To minimize parasitic absorption, the n-type InGaAs absorber and InP layer are 1.7 μ m thick with a dopant concentration of 1 x 10¹⁷ cm⁻³ (see Methods), whereas the heavily p-doped InGaAs (1 x 10¹⁸ cm⁻³) contact layers are shaded by the metal gridlines. For the substrate, we use double-side polished Si that is chemically compatible with the III-V processing protocol (2, 29)

and has a high thermal conductivity of 130 W/m/K at 25°C. Use of intrinsic, float zone Si minimizes free carrier and impurity absorption leading to a low mid-IR extinction coefficient.

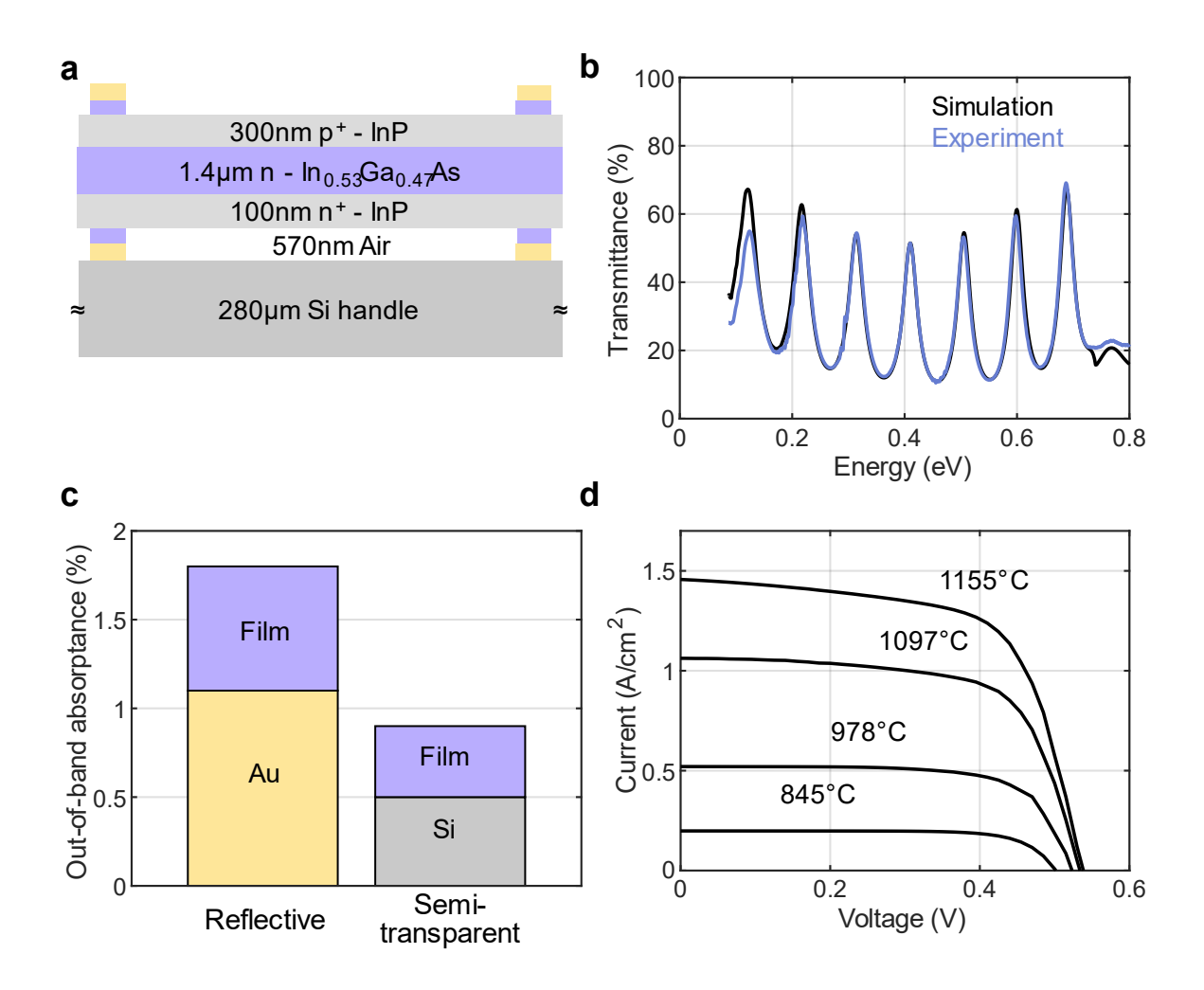


Figure 3. Optical and electrical characterization of the semitransparent cell. (a) Schematic of the fabricated semitransparent cell. This cell consists of a $280\mu m$ thick IR-transparent Si substrate supporting an InGaAs/InP heterojunction cell. (b) Experimental transmittance of the cell (blue), measured by FTIR, matches the simulated transmittance (black) for energies > 0.13 eV. (c) Contributions of active and inactive layers to the total below-bandgap absorptance in the reflective (left) and semitransparent (right) cells. (d) Example illuminated J-V characteristics for the semitransparent cell.

Figure 3b depicts the spectral transmittance of the cell at normal incidence as measured by Fourier transmission IR spectrometry. Experimental transmittance is observed to marginally deviate from

simulation for energies less than 0.13eV. This measurement is paired with the spectral reflectance (see *Supporting Information*) of the semitransparent cell to yield $A_{out} = 0.9\%$, as weighted by emission from a blackbody at 1227°C (1500 K). For reference, a reflective air-bridge control fabricated using the same epitaxial growth exhibits a measured $A_{out} = 1.8\%$ (see *Supporting Information*).

We further utilize transfer matrix optical modeling (31) to estimate the contributions of the Au reflector and the Si substrate in the reflective and semitransparent cells. Figure 3c shows the contributions of the active and inactive layers of each cell to the total below-bandgap absorptance. The Au absorbs 1.1% and the heterostructure absorbs 0.7% in the reflective air-bridge cell. In contrast, the polished Si substrate only absorbs 0.5%. We assign the remaining parasitic absorption (0.4%) to the InGaAs/InP heterostructure. This film is slightly more absorptive than that in previous work (2), which may be attributed to differences in the growth process (metallorganic chemical vapor deposition vs. molecular beam epitaxy) and/or layer thickness differences. Nonetheless, results show that by removing the Au reflector, absorption is substantially reduced, thus demonstrating the fabrication of semitransparent TPV devices with $A_{out} < 1.5\%$.

To characterize the power output and efficiency of the cells, voltage sweeps were performed under illumination by a SiC globar with an ellipsoidal concentrator, as previously (2). Figure 3d depicts a set of illuminated current density-voltage (J-V) characteristics for the semitransparent cell, with T_h ranging from 700°C to 1215°C. Complete experimental data are provided in the *Supporting Information*. Short-circuit current densities, J_{sc} , are in the range of a realistic TPV system (view factor of ~0.75). The voltage factors are higher than our previous work, which is attributed to

improved film quality. The series resistance and saturation dark currents, extracted from fitting both illuminated and dark measurements, show that patterning the rear Au layer slightly increases series resistance. Although not shown, thicker Au gridlines can be used to mitigate this effect.

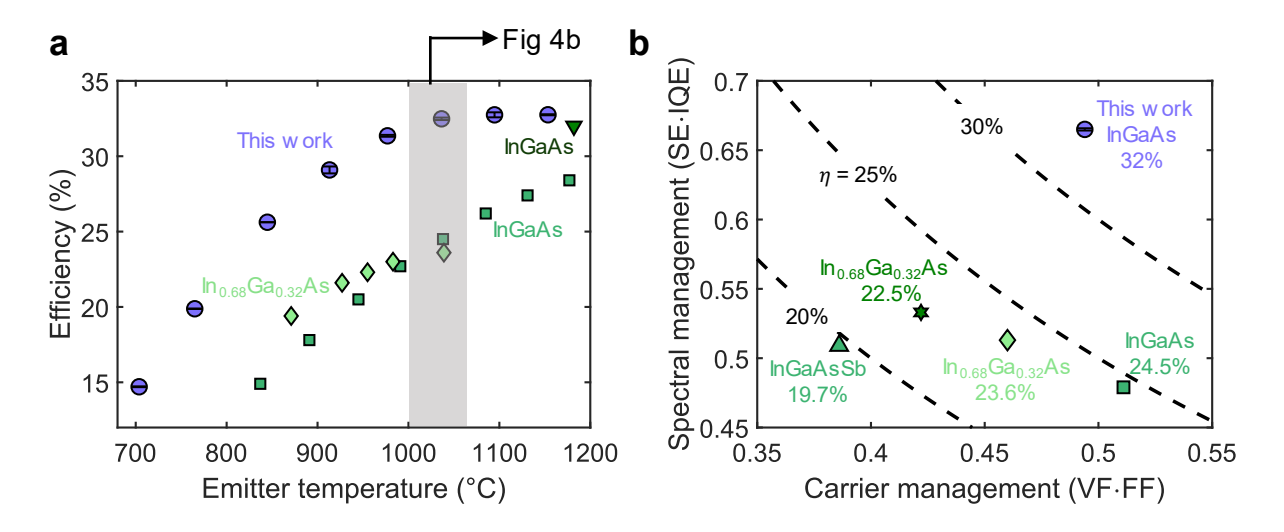


Figure 4. Efficiency of the semitransparent cell. (a) TPV efficiency of the semitransparent (purple) cell as a function of variable emitter temperature (T_h) . The best previously reported measured efficiencies within this T_h range are depicted by the green squares (28), diamonds (27) and downward triangle (2). (b) Spectral management $(SE \cdot IQE)$ as a function of carrier management $(VF \cdot FF)$ for TPV cells in the temperature range of 1000°C-1050°C. Dashed curves represents efficiency benchmarks: square (28), diamond (27), star (32), and upward triangle (33).

Figure 4a shows the TPV efficiency (η_{TPV}) vs. T_h for the semitransparent cell compared to the best previously reported measured efficiencies within this T_h range (2, 27, 28). η_{TPV} is defined as the ratio of power generated to the radiative heat absorbed by the cell (2). The efficiency decreases with decreasing emitter temperature due to the red-shifted emission spectrum, which increases spectral losses at photon energies < 0.13 eV. η_{TPV} also decreases with increasing emitter temperature due to cell heating (see *Supporting Information*). We note that the semitransparent geometry requires lateral heat conduction along the substrate to moderate cell temperature, whereas a reflective cell can be directly cooled from the back. Despite these losses, the

semitransparent cell achieves $\eta_{TPV} = 32.5 \pm 0.1$ % at ~1036°C. This represents an 8% absolute (~33% relative) improvement compared to the prior highest efficiency of 24.5% (28) at comparable emitter temperatures of 1000-1050°C. We also note that the semitransparent cell exhibits a ~6% relative improvement compared to the reflective air-bridge control at ~1036°C (see *Supporting Information*).

To further highlight the improvements relative to state-of-the-art approaches, we separate contributions to the TPV efficiency due to the spectral management and carrier management efficiencies, as shown in Figure 4b. The improved spectral management of the semitransparent design is captured by the relative position of the purple data point along the vertical axis. In addition, the semitransparent device exhibits a high carrier management efficiency, comparable to the best InGaAs devices using conventional metallic reflectors (28). Overall, this result demonstrates that the semitransparent architecture does not compromise carrier management, while providing a substantial gain in spectral management of moderate temperature emission.

Discussion

Here, we use optical and electronic simulations (2, 34) to optimize the design of a symmetric, bifacial semitransparent cell based on the demonstrated device characteristics. The effects of material quality and gridline optimization are modeled by assuming a Shockley-Read-Hall recombination lifetime of $\tau_{SRH} = 47\mu s$, which to our knowledge is the longest reported for InGaAs (35), and a series resistance $R_s = 10 \text{ m}\Omega \text{ cm}^2$, which has been attained for similar patterned dielectric back contact devices (4). The cell is assumed to be 1 cm in length and supported at both ends by a 25°C heat sink. Figure 5a shows the dependence of TPV efficiency on these carrier

management assumptions. Notably, the efficiency of a bifacial semitransparent cell with a 280 μm thick Si substrate is expected to exceed 40% with a 1000°C emitter. Figure 5a further shows the dependence on substrate thickness, which affects both cell temperature and optical performance. The model predicts that thinner substrates (*e.g.*, 100 μm) improve performance at lower emitter temperatures, at which thermal management via heat conduction does not limit performance. In contrast, a 500 μm thick substrate may provide better heat conduction, but it leads to increased parasitic absorptance at long wavelengths, resulting in lower efficiencies within this temperature range.

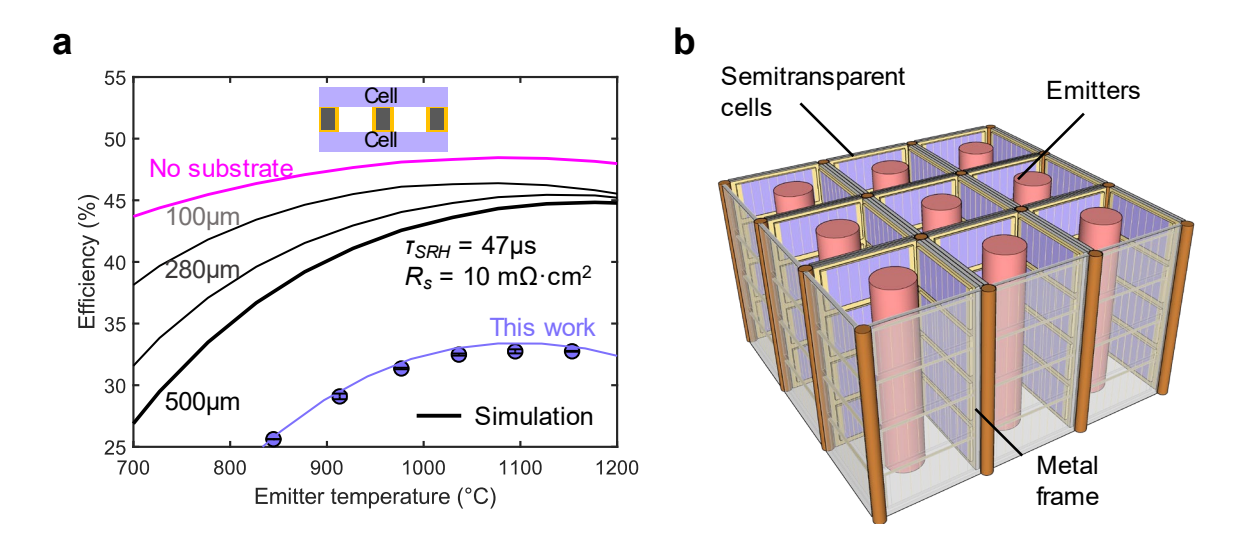


Figure 5. Opportunities in transmissive control. (a) The dashed lines highlight near-term improvements (InGaAs with $R_s = 10 \text{m}\Omega.\text{cm}^2$ and $\tau_{SRH} = 47 \mu \text{s}$) with a Si substrate of varying thickness (in black) and without a substrate (in magenta). The simulation predicts the highest efficiency when the substrate is altogether replaced by mechanically supportive, heat-conducting gridlines, which may enable $A_{out} < 0.5\%$ and negligible temperature gradients. Purple circles represent the experimental efficiency for semitransparent cell demonstrated in this study while the purple dashed line is a simulation of our experimental work. (b) Proposed modular design for interfacing semitransparent cells and emitters. In this geometry, an array of metal fins supports and manages the temperature of the semitransparent cells, which are illuminated by an interlocked array of cylindrical emitters.

Lastly, we explore a design consisting of mechanically supportive, heat conducting grid lines in place of the Si substrate. The gridlines may comprise highly conductive materials such as copper, graphite, or other emerging materials such as cubic boron arsenide (36), and can be coated with Au to reduce optical loss. This configuration has the potential to reduce A_{out} to below 0.5% and enable a peak efficiency of 48.5% at 1000° C, provided that the active semiconductor membrane is the only source of parasitic absorption. Although beyond the scope of this study, we expect that the risks associated with temperature rise of the cell can be mitigated through optimization of geometrical parameters such as aspect ratio and fin thickness. Specifically, the metallic frame can be optimized to remove waste heat and maintain cell temperatures. In Figure 5b, we show that the semitransparent cells can be interdigitated with multiple hot emitters in a cross-flow geometry. Thermally grounding the fins along two edges decreases the heat diffusion path length by a factor of two compared to an open-ended fin, which in turn, decreases temperature rise by a factor of four.

Conclusion

We demonstrated transmissive spectral control as an approach for achieving wavelength-selective radiative transfer in thermophotovoltaic systems that has the potential to overcome the limitations of emissive and reflective methods. The approach features a symmetric device that captures transmitted below-bandgap photons using a secondary thermal emitter situated at the rear, thereby recovering the large amount of power carried by these photons. We fabricated a semitransparent cell with a single, thin InGaAs/InP heterojunction membrane, supported by an intrinsic, float zone Si wafer. Experimental spectral analysis is paired with simulation to decouple contributions to parasitic absorptance in the semitransparent cell. In the temperature range relevant to conversion

of waste, solar, and nuclear generated heat, we demonstrated a 33% relative improvement compared to previously reported efficiencies. Our simulations show that efficiencies as high as 48% could be achieved at 1000°C by optimizing material quality and thermal management within the framework of transmissive spectral control. Overall, we show that this approach to photon management may expand the use of TPVs into a wider range of applications with significant potential to reduce greenhouse gas emissions.

Materials and Methods

Material growth

The heterostructure was epitaxially grown on a 300 μ m thick (100) InP substrate using metalorganic chemical vapor deposition (University Wafer Inc., South Boston, MA, USA). The epitaxial film consists of a 200nm thick Mg-doped (1 x 10^{18} cm⁻³) In_{0.53}Ga_{0.47}As (InGaAs) front contact layer, 300nm Mg-doped (1 x 10^{18} cm⁻³) InP front window layer, 1.4 μ m thick Si-doped (1 x 10^{17} cm⁻³) InGaAs absorber layer, 100 nm Si-doped (1 x 10^{18} cm⁻³) InP rear window layer, and 100nm thick Si-doped (1 x 10^{18} cm⁻³) InGaAs rear contact layer.

Fabrication

All layers are photolithographically patterned using SPR 220 3.0 photoresist (Kayaku Advanced Material Inc., Westborough, MA, USA.). Metal layers are patterned using LOR 10B (Kayaku Advanced Material Inc., Westborough, MA, USA.) and SPR 220 3.0 bilayer photoresist. The epitaxial sample and a Si wafer are soaked in buffered HF for 90s to remove the native surface oxides. The cathode contact grid (10nm Ti / 225nm Au) is deposited by electron-beam evaporation in a chamber with a base pressure of 4x10⁻⁶ torr. Grid lines are 10 μm wide on a 64 μm pitch. The

epitaxial sample is soaked in 1:1:8 H₃PO₄:H₂O₂:H₂O for 20s to remove the 100 nm thick InGaAs rear contact layer in the area between grid lines, while the contact layer beneath the grid lines is protected. Parallel Au patterns on the epitaxial sample and Si wafer (the substrate) are spatially aligned and cold-weld bonded using a flip chip bonder (Finetech) by applying heat (150°C) and pressure (2 MPa) for 5 min. The bond strength is increased at the same temperature and higher pressure (8 MPa) for 10 min using an EVG 510 wafer bonder. The bonded sample is soaked in HCl for 90 min to remove the InP substrate. This process is compatible with non-destructive epitaxial lift-off techniques, which may preserve the expensive InP growth substrate for additional growths (37). The device mesa is etched by alternating soaks in InGaAs (1:1:8 H₃PO₄:H₂O₂:H₂O) and InP (1:1 HCl:H₂O) etchant solutions. The anode contact grid (10 nm Ti / 30 nm Pt / 560 nm Au) is deposited by electron-beam evaporation. The anode contact grid is spatially aligned to the buried cathode contact grid epitaxial layer to shade the absorptive InGaAs contact layers. Lastly, the sample is soaked in 1:1:8 H₃PO₄:H₂O₂:H₂O 60s to remove the 300nm thick InGaAs front contact between the grid lines.

Author Contributions

Cell fabrication: TB, BRL. Cell characterization: TB, BRL, RL. TPV measurements: TB, BRL. Conceptualization: TB, ZB, AL. Funding and project administration: AL, SRF. Supervision: AL, SRF. Writing original draft: TB, BRL, AL. Review and editing: all authors.

Competing Interests

The authors declare no competing financial interest.

Acknowledgments

This material is based upon work supported by the National Science Foundation under Grant Numbers 2018572 and 2144662. TB acknowledges support from Rich and Gabrielle Lesser.

Data availability

All study data are included in the article and/or the SI.

References

- 1. T. C. Narayan, *et al.*, World record demonstration of >30% thermophotovoltaic conversion efficiency in 2020 47th IEEE Photovoltaic Specialists Conference (PVSC), (2020), pp. 1792–1795.
- 2. D. Fan, *et al.*, Near-perfect photon utilization in an air-bridge thermophotovoltaic cell. *Nature* (2020) https://doi.org/10.1038/s41586-020-2717-7.
- 3. T. C. Narayan, *et al.*, Platform for Accurate Efficiency Quantification of >35% Efficient Thermophotovoltaic Cells in *2021 IEEE 48th Photovoltaic Specialists Conference (PVSC)*, (IEEE, 2021), pp. 1352–1354.
- 4. M. K. Arulanandam, *et al.*, GaAs thermophotovoltaic patterned dielectric back contact devices with improved sub-bandgap reflectance. *Sol. Energy Mater. Sol. Cells* **238**, 111545 (2022).
- 5. E. J. Tervo, *et al.*, Efficient and Scalable GaInAs Thermophotovoltaic Devices (2022) https://doi.org/10.48550/arXiv.2207.00565.
- 6. A. LaPotin, et al., Thermophotovoltaic efficiency of 40%. Nature 604, 287–291 (2022).
- 7. A. Licht, N. Pfiester, D. DeMeo, J. Chivers, T. E. Vandervelde, A Review of Advances in Thermophotovoltaics for Power Generation and Waste Heat Harvesting. *MRS Adv.* **4**, 2271–2282 (2019).
- 8. L. Tang, L. M. Fraas, Z. Liu, C. Xu, X. Chen, Performance Improvement of the GaSb Thermophotovoltaic Cells with n-Type Emitters. *IEEE Trans. Electron Devices* **62**, 2809–2815 (2015).
- 9. C. McMillan, "Manufacturing Thermal Energy Use in 2014" (2019) https://doi.org/https://doi.org/10.7799/1570008.
- 10. A. Lenert, *et al.*, A nanophotonic solar thermophotovoltaic device. *Nat. Nanotechnol.* **9**, 126–130 (2014).
- 11. N.-P. Harder, P. W rfel, Theoretical limits of thermophotovoltaic solar energy conversion. *Semicond. Sci. Technol.* **18**, S151–S157 (2003).
- 12. C. Ungaro, S. K. Gray, M. C. Gupta, Solar thermophotovoltaic system using nanostructures. *Opt. Express* **23**, A1149–A1156 (2015).
- 13. E. Rephaeli, S. Fan, Absorber and emitter for solar thermo-photovoltaic systems to achieve efficiency exceeding the Shockley-Queisser limit. *Opt. Express* **17**, 15145 (2009).
- 14. Z. Zhou, E. Sakr, Y. Sun, P. Bermel, Solar thermophotovoltaics: reshaping the solar spectrum. *Nanophotonics* **5**, 1–21 (2016).
- 15. Y. Wang, H. Liu, J. Zhu, Solar thermophotovoltaics: Progress, challenges, and opportunities. *APL Mater.* **7**, 080906 (2019).
- 16. D. M. Bierman, *et al.*, Enhanced photovoltaic energy conversion using thermally based spectral shaping. *Nat. Energy* **1**, 16068 (2016).
- 17. R. Bhatt, I. Kravchenko, M. Gupta, High-efficiency solar thermophotovoltaic system using a nanostructure-based selective emitter. *Sol. Energy* **197**, 538–545 (2020).
- 18. D. Wilt, D. Chubb, D. Wolford, P. Magari, C. Crowley, Thermophotovoltaics for Space Power Applications. *AIP Conf. Proc.* **890**, 335–345 (2007).
- 19. T. Burger, C. Sempere, B. Roy-Layinde, A. Lenert, Present Efficiencies and Future Opportunities in Thermophotovoltaics. *Joule* **4**, 1660–1680 (2020).
- 20. R. Sakakibara, *et al.*, Practical emitters for thermophotovoltaics: a review. *J. Photonics Energy* **9**, 1–20 (2019).

- 21. M. C. Gupta, C. Ungaro, J. J. Foley, S. K. Gray, Optical nanostructures design, fabrication, and applications for solar/thermal energy conversion. *Sol. Energy* **165**, 100–114 (2018).
- 22. M. Shimizu, A. Kohiyama, H. Yugami, Evaluation of thermal stability in spectrally selective few-layer metallo-dielectric structures for solar thermophotovoltaics. *J. Quant. Spectrosc. Radiat. Transf.* **212**, 45–49 (2018).
- 23. S. Bitnar, *et al.*, Practical thermophotovoltaic generators. *Semiconductors* **38**, 941–945 (2004).
- 24. S. McSherry, *et al.*, Nanophotonic control of thermal emission under extreme temperatures in air. *Nat. Nanotechnol.* (2022) https://doi.org/10.1038/s41565-022-01205-1.
- 25. M. Chirumamilla, *et al.*, Thermal stability of tungsten based metamaterial emitter under medium vacuum and inert gas conditions. *Sci. Rep.* **10**, 3605 (2020).
- 26. R. M. Swanson, Recent developments in thermophotovoltaic conversion. *1980 Int. Electron Devices Meet.*, 186–189 (1980).
- 27. B. Wernsman, *et al.*, Greater than 20% radiant heat conversion efficiency of a thermophotovoltaic radiator/module system using reflective spectral control. *IEEE Trans. Electron Devices* **51**, 512–515 (2004).
- 28. Z. Omair, *et al.*, Ultraefficient thermophotovoltaic power conversion by band-edge spectral filtering. *Proc. Natl. Acad. Sci.* **116**, 15356–15361 (2019).
- 29. T. Burger, D. Fan, K. Lee, S. Forrest, A. Lenert, Thin-Film Thermophotovoltaic Cells with High Spectral Selectivity (2018).
- 30. B. Lee, *et al.*, Air-Bridge Si Thermophotovoltaic Cell with High Photon Utilization. *ACS Energy Lett.* 7, 2388–2392 (2022).
- 31. X.-H. Deng, J.-T. Liu, J.-R. Yuan, Q.-H. Liao, N.-H. Liu, A new transfer matrix method to calculate the optical absorption of graphene at any position in stratified media. *Europhys. Lett.* **109**, 27002 (2015).
- 32. D. N. Woolf, *et al.*, High-efficiency thermophotovoltaic energy conversion enabled by a metamaterial selective emitter. *Optica* **5**, 213–218 (2018).
- 33. M. W. Dashiell, *et al.*, Quaternary InGaAsSb Thermophotovoltaic Diodes. *IEEE Trans. Electron Devices* **53**, 2879–2891 (2006).
- 34. B. Roy-Layinde, *et al.*, Sustaining efficiency at elevated power densities in InGaAs airbridge thermophotovoltaic cells. *Sol. Energy Mater. Sol. Cells* **236**, 111523 (2022).
- 35. R. K. Ahrenkiel, R. Ellingson, S. Johnston, M. Wanlass, Recombination lifetime of In 0. 53 Ga 0. 47 As as a function of doping density. **72**, 3470–3472 (1998).
- 36. S. Yue, *et al.*, High ambipolar mobility in cubic boron arsenide revealed by transient reflectivity microscopy. *Science* (80-.). **377**, 433–436 (2022).
- 37. K. Lee, J. D. Zimmerman, T. W. Hughes, S. R. Forrest, Non-Destructive Wafer Recycling for Low-Cost Thin-Film Flexible Optoelectronics. 4284–4291 (2014).

Supplementary information

Semitransparent thermophotovoltaics for efficient utilization of moderate temperature thermal radiation

Tobias Burger^{1,+}, Bosun Roy-Layinde^{1,+}, Rebecca Lentz², Zachary Berquist¹,

Stephen R. Forrest^{2,3,4}, and Andrej Lenert^{*,1}

¹Department of Chemical Engineering

²Department of Electrical Engineering and Computer Science

³Department of Materials Science and Engineering

⁴Department of Physics

University of Michigan, Ann Arbor, MI, 48109, USA

⁺These authors contributed equally: Tobias Burger, Bosun Roy-Layinde

*Corresponding author: <u>alenert@umich.edu</u>

This PDF file includes:

Supporting text

Supplementary Figures 1 to 4

Supplementary Table 1

S1 Reflectance and transmittance measurement:

Reflectance of the semitransparent and control cells are measured using an Agilent Cary 620 FTIR microscope with incidence angles in the range of 18-41°. The reflectance for both cells is also simulated using transfer matrix methods. The absorptance of the semitransparent cell is calculated from this reflectance measurement and the transmittance measurement in Figure 3b. Figure S1 depicts these reflectance measurements and simulation.

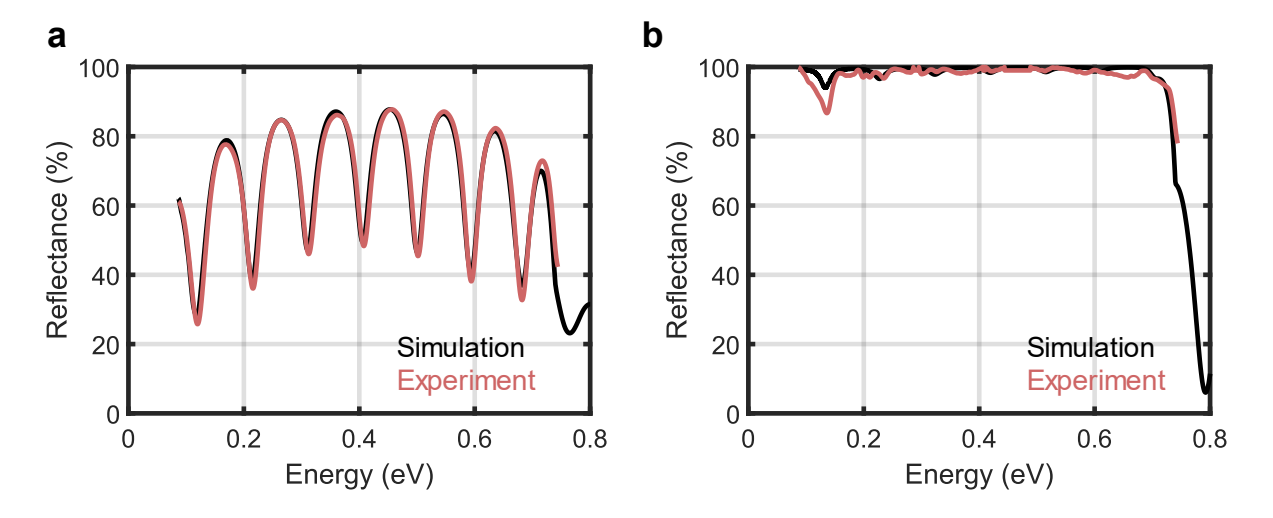


Figure S1. Reflectance measurements and simulations for the semitransparent (left) and reflective air-bridge control (right).

S2 Current-voltage (*J-V*) characteristics:

Table S2 depicts the complete experimental J-V (V_{oc}, J_{sc}, and FF) dataset for the semitransparent cell.

Table S1. Measured *J-V* properties of the semitransparent cell vs. emitter temperature.

T_h (°C)	J_{SC} (mA/cm ²)	V_{OC} (mV)	FF (%)
704	54.72	470.28	75.96
765	99.61	485.88	76.01

845	255.46	508.07	73.84
913	369.57	515.65	72.37
978	516.52	522.74	70.84
1036	710.84	529.05	69.20
1097	1062.17	534.75	66.72
1155	1457.11	538.62	64.81
1212	1959.57	541.76	63.57

The maximum power increases with temperature (Figure S2). This increase in power leads to a rise in heat load leading to the increase in cell temperature. We describe the thermal management approach below.

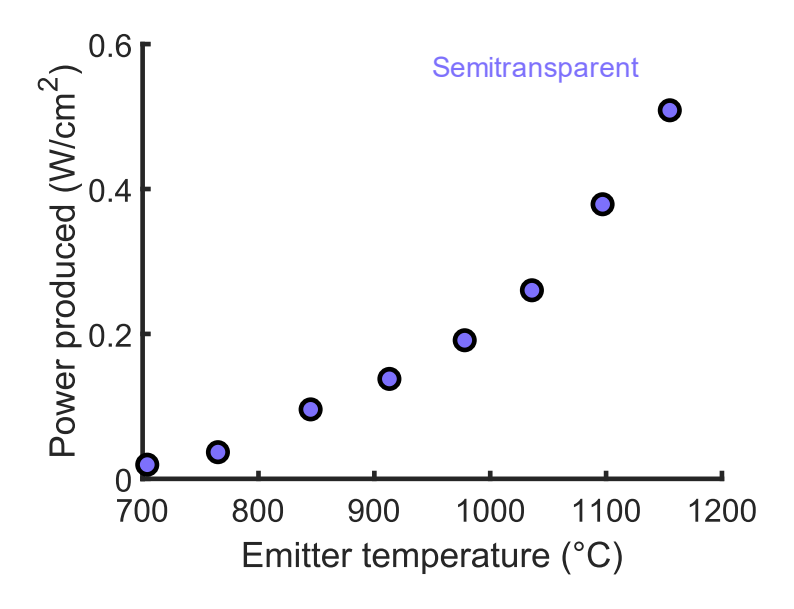


Figure S2. Maximum power produced for the semitransparent cell as a function of variable emitter temperature.

S3 Thermal management:

Figure S3 (left) depicts the anticipated temperature profile along the length of a semitransparent cell for an emitter temperature of 1200°C and a view factor of 100%. The temperature of the active region is expected to be slightly higher (+0.5°C) than the substrate temperature due to thermal resistance across the air-gap. The average cell (junction) temperature for this illumination condition is 29°C. Figure S3 (right) shows that a 500 μm thick substrate may provide better heat conduction, therefore mitigating cell heating losses at high emitter temperatures. However, this also increases parasitic absorptance at long wavelengths, resulting in lower efficiencies at moderate temperatures, for which more below-bandgap photons are emitted and the thermal load is reduced. This result depends on the heat conduction path length of the cell.

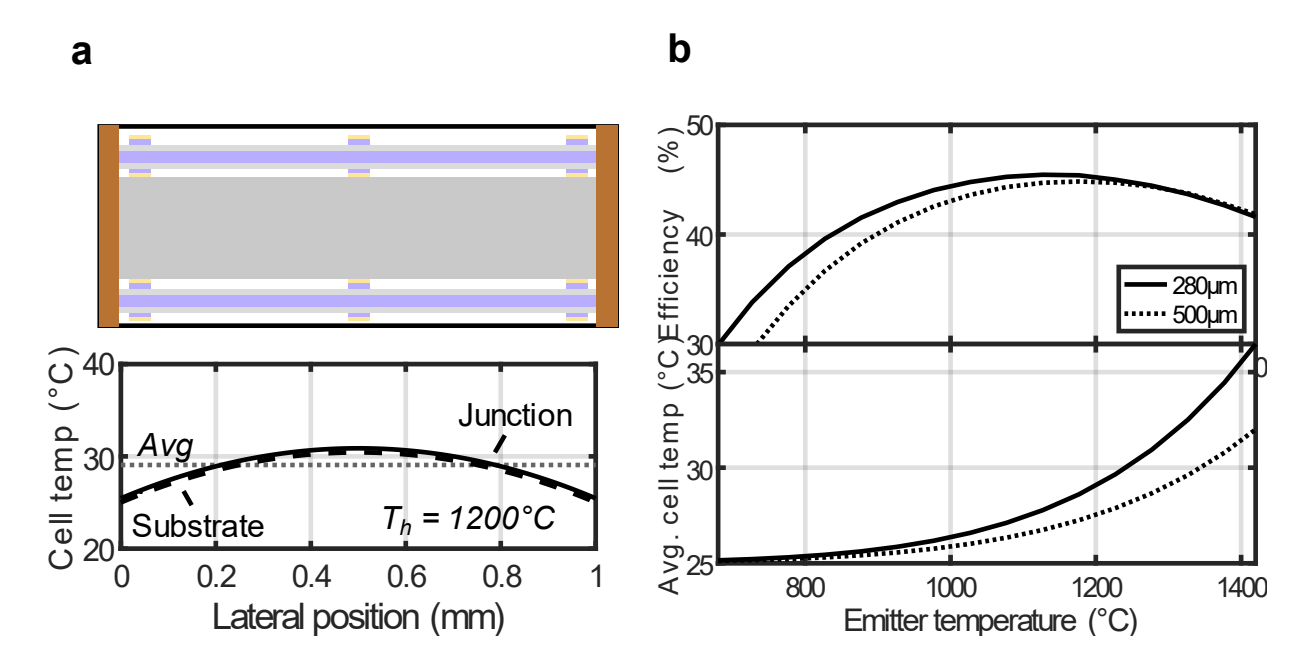


Figure S3. Substrate geometry effects on cell temperature, optical loss, and efficiency. (a) Anticipated temperature profile of a 1-cm long semitransparent cell illuminated by a 1200°C blackbody emitter. Junction temperature (solid curve) is slightly higher than substrate temperature (dashed curve) because of the thermal resistance of the air gap. (b) Average cell temperature and predicted efficiency as a function of emitter temperature for a semitransparent cell with a 280μm (solid curve) and a 500μm (dashed curve) Si substrate.

Cell heating effects

Cell heating effects for the semitransparent cell assume a temperature coefficient of β_{η} = -0.16%/K, based on the anticipated T_c at the given T_h . The temperature coefficient of the semitransparent cell is determined through characterization of the cell power output for a range of cell temperatures, as previously (2). The temperature profile is calculated from the anticipated thermal load at each T_h using a one-dimensional heat conduction model with a volumetric heat generation term.

S4 Reflective control:

The performance of the semitransparent cell is benchmarked against a reflective air-bridge control. As shown in Figure S4, the semitransparent cell out-performs the reflective cell for moderate emitter temperatures. This efficiency gap narrows with decreasing T_h , however, because the Si substrate absorbs at energies below 0.13eV.

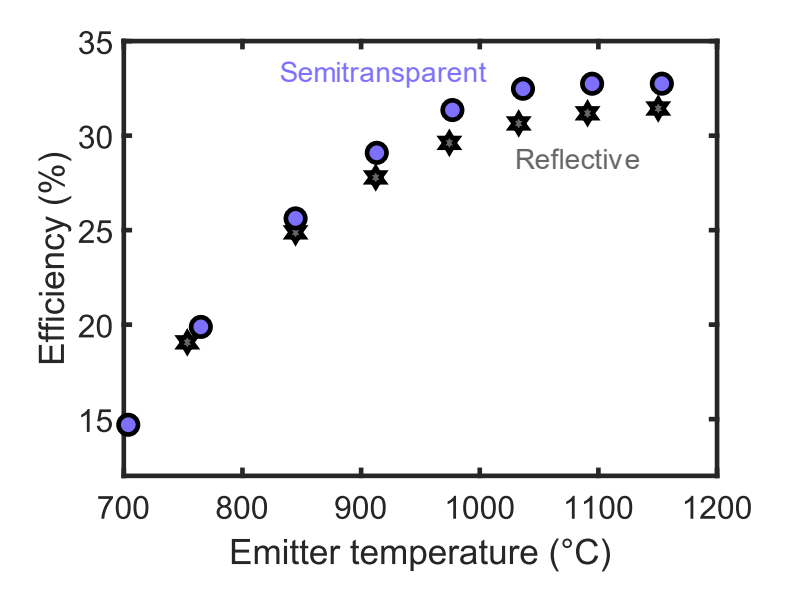


Figure S4. Power conversion efficiency of the semitransparent (purple) and reflective air-bridge control (gray) cells as a function of variable emitter temperature.

References

- 1. K. Lee, J. D. Zimmerman, T. W. Hughes, S. R. Forrest, Non-Destructive Wafer Recycling for Low-Cost Thin-Film Flexible Optoelectronics. 4284–4291 (2014).
- 2. B. Roy-Layinde, *et al.*, Sustaining efficiency at elevated power densities in InGaAs airbridge thermophotovoltaic cells. *Sol. Energy Mater. Sol. Cells* **236**, 111523 (2022).